Ultrasound attenuation and texture analysis of diffuse liver disease: methods and preliminary results

Phys. Med. Biol., 1991, Vol. 36, No 8, 1039–1064. Printed in the UK

Ultrasound attenuation and texture analysis of diffuse liver disease: methods and preliminary results

B J Oosterveld, J M Thijssen, P C Hartman†, R L Romijn‡ and G J E Rosenbusch

University Hospital, PO Box 9101, 6500 HB Nijmegen, The Netherlands

Received 12 November 1990

Abstract. A study was performed to find and test quantitative methods of analysing echographic signals for the differentiation of diffuse liver diseases. An on-line data acquisition system was used to acquire radiofrequency (RF) echo signals from volunteers and patients. Several methods to estimate the frequency-dependent attenuation coefficient were evaluated, in which a correction for the frequency and depth-dependent diffraction and focusing effects caused by the sound beam was applied. Using the estimated value of the attenuation coefficient the RF signals themselves were corrected to remove the depth dependencies caused by the sound beam and by the frequency-dependent attenuation. After this preprocessing the envelope of the corrected RF signals was calculated and B-mode images were reconstructed. The texture was analysed in the axial direction by first- and second-order statistical methods.

The accuracy and precision of the attenuation methods were assessed by using computer simulated RF signals and RF data obtained from a tissue-mimicking phantom. The phantom measurements were also used to test the performance of the methods to correct for the depth dependencies. The echograms of 163 persons, both volunteers and patients suffering from a diffuse liver disease (cirrhosis, hepatitis, haemochromatosis), were recorded. The mutual correlations between the estimated parameters were used to preselect parameters contributing independent information, and which can subsequently be used in a discriminant analysis to differentiate between the various diseased conditions.

1. Introduction

Based on the experience from *in-vitro* experiments with liver specimens (Cloostermans and Thijssen 1983, Cloostermans *et al* 1986) and from extensive computer simulations using realistic three-dimensional tissue and transducer models (Verhoef *et al* 1985, Oosterveld *et al* 1985), we have performed a clinical study on the characterization of the liver by quantitative analysis of radiofrequency (RF) ultrasound signals. Since the methods were not designed for the detection of focal lesions we have confined ourselves to diffuse liver diseases, in which it was assumed that changes had affected the whole organ.

Other investigators have reported on the results of their clinical studies concerning diffuse liver disease, using attenuation measurements (Taylor *et al* 1986, Garra

† Present address: Elkerliek Hospital, Deurne, The Netherlands.

‡ Present address: Canisius Wilhelmina Hospital, Nijmegen, The Netherlands.

0031-9155/91/081039+26$03.50

et al 1987a, b, Parker *et al* 1988) as well as the analysis of the B-mode texture (Reath *et al* 1985, Nicholas *et al* 1986, Insana *et al* 1986, Morris 1988). Most procedures for the estimation of the attenuation coefficient employ some corrections for the depth-dependent properties of the sound beam, which would otherwise influence the estimation (Cloostermans *et al* 1986, Verhoef *et al* 1985, Insana 1983, Fink and Cardoso 1984).

The sound beam, however, also causes a depth dependence of the B-mode image texture. Correction of the image (Zuna *et al* 1987) or correction of the parameters from texture analysis (Morris 1988) for this influence, has only been attempted in a simple way. Usually however, the analysis is confined to a region of interest (ROI) that has a fixed distance to the transducer (Raeth *et al* 1985, Nicholas *et al* 1986). In this way not only the influence of the sound beam is reduced, but also the flexibility in the choice of the ROI. Furthermore, this method does not reduce the influence that the attenuation has on the texture (Oosterveld *et al* 1985) and, finally, the results obtained cannot easily be generalized.

The texture analysis methods range from well known methods designed primarily for optical images (Raeth *et al* 1985, Nicholas *et al* 1986, Morris 1988) to methods which are based on realistic models of the liver tissue and a deeper theoretical insight in the acoustical interactions between the tissue and the interrogating sound pulses (Insana *et al* 1986, Wagner *et al* 1986).

We have designed a method to produce B-mode scans from the RF signals, which are first corrected for the diffraction and focusing effects and for the depth dependencies caused by attenuation. To investigate the potentials of our method we have performed a retrospective clinical study. We have scanned a group of patients having liver cirrhosis, most of which proven by biopsy, and a group of volunteers who had a normal liver. We used a measurement set-up that enabled us to digitize and store the RF signals corresponding to a region of interest, obtained *in vivo*. Several methods to estimate the attenuation coefficient were employed. From the corrected envelope of the RF signals texture parameters were estimated. The discriminating power of the obtained echographic parameters was investigated by applying a Student t-test.

2. Analysis of the echo signals

2.1. Diffraction correction: theoretical background

The echoes received by the transducer are the result of the linear accumulation of backscatterings from inhomogeneities in the tissue. The signal as it is observed depends on the transducer geometry and the properties of the interrogated medium. This can be described by various complex transfer functions, of which the following can be distinguished:

(i) $P(f)$ the electroacoustic round-trip transfer function of the piezoelectric material of the transducer, which is involved in the conversion of electric energy to acoustic energy and *vice versa*;

(ii) $S(f)$ the average backscattering coefficient of the tissue inhomogeneities, which is assumed to be constant in the region of interest (homogeneous and isotropic); and

(iii) $H_t'(f,\boldsymbol{r}), H_r'(f,\boldsymbol{r})$ the transfer functions associated with the impulse response function of the transducer at position $\boldsymbol{r}$ (figure 1), in transmission and reception, respectively.

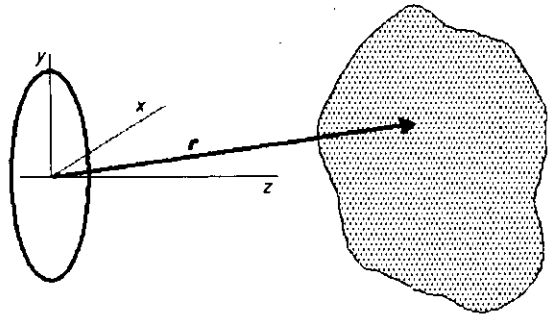

Figure 1. Transducer and tissue in a Cartesian coordinate system.

These latter transfer functions depend on the transducer geometry (focusing and aperture diffraction) and the propagation characteristics of the medium. If the point $\boldsymbol{r}$ is approximately equidistant to all points of the transducer aperture (i.e. the far field approximation), these transfer functions may be separated into a tissue transfer function A and a diffraction transfer function H:

$$H_t'(f,\boldsymbol{r}) = H_t(f,\boldsymbol{r})A(f,r) \tag{1}$$

$$H_r'(f,\boldsymbol{r}) = H_r(f,\boldsymbol{r})A(f,r). \tag{2}$$

The functions $H_t(f,\boldsymbol{r})$ and $H_r(f,\boldsymbol{r})$ relate to the impulse response functions in a lossless medium and are identical due to the validity of reciprocity in the pulse-echo mode. Therefore, the subscripts can be omitted.

A general description of the tissue transfer function is given by

$$A(f,r) = \exp[-\mu(f)r] \tag{3}$$

where the attenuation coefficient μ is expressed in neper cm^{-1}, and

$$\alpha(f) = \frac{20}{\ln 10}\mu(f) \doteq 8.686\mu(f) \tag{4}$$

where $\alpha(f)$ is expressed in dB cm^{-1}. Using the described transfer functions the spectrum of the echo signal due to one scatterer at position $\boldsymbol{r}$ can be described by

$$\begin{aligned} E(f) &= P(f)H_t'(f,\boldsymbol{r})S(f)H_r'(f,\boldsymbol{r}) \\ &= P(f)H^2(f,\boldsymbol{r})A^2(f,r)S(f). \end{aligned} \tag{5}$$

If there is more than one inhomogeneity present in the tissue the resulting echo signal is the linear summation of the individual echoes. In the frequency domain this results in

$$\begin{aligned} E(f) &= \sum_j E_j(f) \\ &= P(f)S(f)\sum_j H^2(f,\boldsymbol{r}_j)A^2(f,r_j) \\ &= P(f)S(f)\sum_j H^2(f,\boldsymbol{r}_j)\exp[-2\mu(f)r_j] \end{aligned} \tag{6}$$

where j is the index of the scatterer at position r_j, provided that the backscattering function $S(f)$ is the same for all inhomogeneities. If only a small time portion of the echo signal is considered the individual echoes will arise at inhomogeneities in a small volume (isochronous volume) at an axial distance z from the transducer, which corresponds to the product of sound velocity c and half of the travel time t. The distances r_j are approximately equal to this depth z and therefore the attenuation factor can be approximated by $\exp[-2\mu(f)z]$. The diffraction transfer function can also be approximated by an average transfer function dependent on depth, $H(f,z)$. The echo signal from an isochronous volume at depth z can now be written as

$$E(f,z) = P(f)S(f)H^2(f,z)\exp[-2\mu(f)z]. \tag{7}$$

From this equation it is clear that a depth independent estimation of the attenuation is only possible if the average transfer function due to diffraction and focusing $H^2(f,z)$ is known.

The texture of the envelope image also shows a depth dependence which is not only caused by the sound beam but by the attenuation as well (Oosterveld *et al* 1985). In the lateral direction the speckle size is inversely proportional to the centre frequency of the propagating pulse, which decreases with depth, due to attenuation. If the pulse has a Gaussian-shaped envelope the speckle size in the axial direction is not influenced by attenuation. The reason for this is that the axial speckle size is dependent on the bandwidth of the propagating pulse only, which is preserved in this special case of a linear-with-frequency attenuation coefficient (Ferrari and Jones 1985). If, however, the pulse shape is not approximately Gaussian, a correction for the attenuation has to be carried out as well for the axial envelope characteristics to become depth independent.

The diffraction transfer function can be estimated by recording RF signals from a tissue mimicking phantom placed in a watertank. If the method outlined in section 3.2 is used, the spectra of the RF signals corresponding to a number of depth segments Δz at distances z_i, for $i = 1,\ldots,n$, from the transducer (i.e. the spectrogram) are obtained such that the depth segments overlap by 50% ($z_i = z_{i-1} + \frac{1}{2}\Delta z$). The resulting amplitude spectrogram is the average diffraction filter transfer function multiplied by the transfer function $S_{\mathrm{ph}}(f)$ of the scatterers within the phantom and by the electroacoustic transfer function $P(f)$ of the transducer

$$E_{\mathrm{ph}}(f,z_i) = P(f)S_{\mathrm{ph}}(f)H^2(f,z_i) \tag{8}$$

where $i = 1,\ldots,n$.

If the spectrogram given by equation (8) is normalized with respect to the spectrum obtained in the focal zone ($z_i = F$) this results in

$$\begin{aligned} H_c^2(f,z_i) &= \frac{E_{\mathrm{ph}}(f,z_i)}{E_{\mathrm{ph}}(f,F)} \\ &= \frac{P(f)S_{\mathrm{ph}}(f)H^2(f,z_i)}{P(f)S_{\mathrm{ph}}(f)H^2(f,F)} \\ &= \frac{H^2(f,z_i)}{H^2(f,F)} \end{aligned} \tag{9}$$

the diffraction transfer function normalized with respect to the focal zone. The normalization thus removes the properties of the tissue phantom. This normalized diffraction

transfer filter $H_c^2(f, z_i)$ represents the change of the spectral content of the RF echo signals due to the depth dependence caused by diffraction and focusing. Correction of a depth segment of a RF signal, e.g. obtained *in-vivo*, is performed by dividing its spectrum by the normalized spectrum of the filter corresponding to the same depth.

2.2. Estimation of the attenuation

Amplitude spectra were calculated using the depth segments of each RF line corresponding to the same distances to the transducer as previously mentioned. Prior to the Fourier transformations the segments were multiplied by a Hanning window (Oppenheim and Schafer 1975). The spectrogram was obtained by ensemble averaging the amplitude spectra at each depth over the RF lines of the ROI (cf equation (7)):

$$E(f, z_i) = P(f)S(f)H^2(f, z_i)\exp[-2\mu(f)z_i] \tag{10}$$

where $i = 1, \ldots, n$ with n the number of 50% overlapping depth segments in the ROI. Correction of this spectrogram with the correction filter of equation (9) yielded

$$\begin{aligned} E_c(f, z_i) &= E(f, z_i)/H_c^2(f, z_i) \\ &= P(f)S(f)H^2(f, F)\exp[-2\mu(f)z_i]. \end{aligned} \tag{11}$$

Since $P(f)S(f)H^2(f, F)$ is independent of depth, equation (11) can be used to find $\mu(f)$ once $E_c(f, z_i)$ is known for a range of depth segments in the tissue.

Several approaches were used to estimate the attenuation coefficient from the corrected spectrogram of equation (11). All these methods are based on the assumption that the interrogated medium is homogeneous. In the multi-narrowband (MNB) approach (Cloostermans and Thijssen 1983) a two-step linear fit method is employed. To the logarithmic (base 10) spectral values at each frequency f_k, $(k = 1, \ldots, K)$ in the usable bandwidth, straight lines are fitted with respect to depth z_i. This yields the attenuation coefficient as a function of frequency $\alpha(f_k)$, $(k = 1, \ldots, K)$ (cf equation (4)). Fits were applied to these values with respect to frequency, corresponding to three models for the frequency dependence of $\alpha(f)$:

(1) $\alpha(f) = \alpha_0 + \alpha_1 f$, a linear fit (MNB);

(2) $\alpha(f) = \beta f$, a linear fit, forced to have zero intercept (MNB_0);

(3) $\alpha(f) = \alpha f^n$, a linear fit through the logarithm of the attenuation coefficient values (MNB_p), yielding α as the value at 1 MHz and n as the slope of this fit.

The MNB method is similar to the spectral-difference method (Kuc and Schwartz 1979), but provides a more efficient use of the echo data.

If the attenuation coefficient is assumed to be linear with frequency, $\alpha(f) = \beta f$, the centroid frequency shift (CFS) method (or spectral shift method) (Kak and Dines 1978, Kuc *et al* 1976, Fink *et al* 1983, Shaffer *et al* 1984) can be applied by estimating the central frequency f_c (i.e. the first order spectral moment) against depth from the corrected spectrogram. The slope of the attenuation coefficient β then follows from the slope of a linear fit to these values against depth,

$$\beta = -\frac{8.686}{2\sigma_f^2}\frac{\Delta f_c}{\Delta z} \qquad (\text{dB cm}^{-1}\ \text{MHz}^{-1}) \tag{12}$$

where σ_f is the standard deviation of the Gaussian amplitude spectra averaged over all depths and $\Delta f_c/\Delta z$ is the slope of the fitted line. For the log-power decay (LPD)

method (or: quasi-narrowband method) (Taylor *et al* 1986, Cloostermans *et al* 1986) the amplitude spectra against depth were squared and integrated over the frequency to yield the zeroth-order power spectral moments (M_0), after which the logarithm (base 10) was taken. The slope of the attenuation coefficient was then estimated using

$$\beta = -\frac{1}{4\bar{f}_c}\frac{\mathrm{d}\log M_0(z)}{\mathrm{d}z} \qquad (\mathrm{dB\ cm^{-1}\ MHz^{-1}}) \tag{13}$$

where $\bar{f}_c$ = the average central frequency in the ROI. A straight line was fitted through the log power values plotted against depth and the slope of this line divided by the central frequency, averaged over all depths, resulted in another estimate of the slope of the attenuation coefficient β. For the MNB and MNB_p methods less strict assumptions are made and, therefore, more general information may be extracted about the tissue.

If a homogeneous medium is considered and the spectral amplitude at each frequency is assumed to be Rayleigh distributed, then the variance of the estimate of the attenuation coefficient can be derived (Kuc 1985, Berger *et al* 1987):

$$\sigma_\beta^2 = \frac{18c\sigma_r^2}{(1-o)^2(WL_w)^3n^3(1-n^{-2})N} \tag{14}$$

where c = speed of sound, σ_r^2 = relative variance of the spectral amplitude = 5.61 dB, W = usable bandwidth, L_w = window length, o = window overlap expressed as a fraction of the window length, n = number of windows, and N = number of independent scan lines.

2.3. Calculation of the envelope of the corrected RF signals

The most rigorous way to remove all the influences of the applied transducer from the RF signals would be by inverse filtering for its depth-dependent point-spread function. This would involve two-dimensional deconvolutions in a number of depth segments of the image. The result of performing such an operation on a RF sector scan would be an image of the scattering inhomogeneities not obscured by speckle. Jeurens *et al* (1987) investigated this procedure and concluded that it would only produce satisfying results if the data could meet certain high quality requirements. Since the data recorded with our equipment (see section 3.1) did not meet these demands we restricted ourselves to correcting the RF signals for those influences that cause a depth dependence of the B-mode lines in the depth direction only. That is, we compensated for depth-dependent diffraction and focusing effects, as well as for the attenuation, in the frequency domain (cf equation (9)). The latter correction was neccessary, because of the non-Gaussian shape of the spectrum of the pulse of our transducer.

Having found the value of the attenuation coefficient the envelope of the RF signals, corrected for the diffraction effects and for the attenuation, was calculated. We proceeded line by line in the same way as with the calculation of the spectrogram, that was used for the estimation of the attenuation, by using 50% overlapping depth segments. Each segment was multiplied by a Hanning window and then the amplitude and phase spectra were calculated by using a fast Fourier transform algorithm (FFT). These were corrected for the diffraction (cf equation (9)) and the attenuation. This preprocessing was comprised in a compound complex transfer function:

$$E_c(f, z_i) = |E_c(f, z_i)|\exp[\mathrm{i}\phi_c(f, z_i)] \tag{15}$$

where

$$|E_c(f, z_i)| = |E(f, z_i)| \frac{\exp[\beta f(z_i - z_0)]}{|H_c^2(f, z_i)|} \tag{16}$$

$$\phi_c(f) = \phi(f) - \frac{2\beta f(z_i - z_0)}{\pi} \{\ln(2\pi f) - \tau_m\} \tag{17}$$

and depth z_0 corresponds to a specific distance from the transducer, for example corresponding to the boundary of the liver. The correction applied to the phase spectrum (equation (17)) was obtained using the causal attenuation model derived by Gurumurthy and Arthur (1982). As proposed by these authors we have taken the minimum-phase delay factor τ_m to be equal to 20.0. Complex demodulation was performed in the frequency domain. The spectrum of the complex pre-envelope was calculated by multiplying the positive frequency part of equation (16) by two and making the negative frequency part equal to zero (Whalen 1971). The resulting spectra were then transferred back to the time domain (pre-envelope) which, after taking the absolute value, yielded the envelope of the segment. Interpolation between the consecutive overlapping segments was neatly performed by the Hanning data window that was applied prior to the calculation of the spectra. Therefore, the resulting envelope segments could simply be added, taking into account the appropriate time delays. By using this approach only a correction in the axial direction was accomplished. In other words, the speckles still showed depth dependence in the lateral direction, although some change of the texture was evident. For this reason the second-order analysis of the image texture was confined to the axial direction only.

2.4. Analysis of the axial texture

First- and second-order texture analysis methods were used, to extract quantitative information from the resulting B-mode images. The first-order statistics characterize the histogram of the echo amplitudes. Two parameters were estimated from the histogram: the average echo amplitude (μ) and the average amplitude divided by the standard deviation (signal-to-noise ratio, SNR $= \mu/\sigma$). For a scattering medium that contains homogeneously distributed and randomly positioned scatterers with a high number density a value of 1.91 is expected for the SNR, which corresponds to a histogram that approximates a Rayleigh probability density function. Deviations from this limiting situation are expected if the density of scatterers is low (sub-Rayleigh) (Oosterveld *et al* 1985) or if a part of the scatterers is regularly spaced (i.e. structure is present) (Wagner *et al* 1988). The average amplitude (μ) depends on the strength of the scatterers and on the square root of the number density of the scatterers (Oosterveld *et al* 1985).

The second-order statistics were confined to the axial autocovariance function and its Fourier transform, namely the power spectrum, of the echo intensity. The full width at half maximum (FWHM) of the autocovariance function was used as an estimate of the average size of the speckles in the axial direction.

In some biological tissues two kinds of scatterers may be distinguished in addition to reflecting boundaries of organs and blood vessels (Insana *et al* 1986). The first kind are randomly positioned scatterers with a high number density, which cannot be resolved by the transducer. The second kind are scatterers which are positioned in a more or less regular order with average spacing $\bar{d}$. These scatterers, therefore,

are structured and the periodicity may or may not be resolved by the transducer. As an example the liver can be considered. The liver cells are organized in lobules, cylindrical structures with a diameter of approximately 1 mm. Because the cells and capillaries are randomly positioned within the lobules they cause random scattering. The spaces between the lobules (triads of Kiernan) are collagen rich, and constitute a more or less regular hexagonal structure. Since collagen is a strongly scattering medium this structure may cause 'structural scattering'.

Following the unified approach of Wagner *et al* (1986) and Insana *et al* (1986) the intensity contributions due to structure (I_s) and due to random (or diffuse) scattering (I_d) were estimated. The intensity due to structure is subdivided into a constant part ($\bar{I}_s$) representing the unresolvable part of the structure and a variable part ($\sigma(I_s)$) representing the resolvable part. $\bar{I}_s$, $\sigma(I_s)$ and I_d were estimated from the autocorrelation function of the intensity and from its Fourier transform, the power spectrum. Refering to figure 2 and using the notation of these authors, the following parameters of the autocorrelation function, $R_I(\Delta z)$, were distinguished

$$t = R_I(0) = \overline{I^2} = 2I_d^2 + 4I_d\bar{I}_s + \overline{I_s^2} = 2\sigma_R^2 + \overline{I_s^2} \tag{18}$$

$$p = R_I(nd) = I_d^2 + 2I_d\bar{I}_s + \overline{I_s^2} = \sigma_R^2 + \overline{I_s^2} \tag{19}$$

$$b = R_I(\infty) = \bar{I}^2 = I_d^2 + 2I_d\bar{I}_s + \bar{I}_s^2 = \sigma_R^2 + \bar{I}_s^2 \tag{20}$$

where $\sigma_R^2 = I_d^2 + 2I_d\bar{I}_s$ is the Rician variance, and p is the value of maximum structured correlation.

From equations (18) and (20) and the definition of the variance of the intensity due to structure, $\sigma^2(I_s) = \overline{I_s^2} - \bar{I}_s^2$, it follows that

$$\sigma^2(I) = \overline{I^2} - \bar{I}^2 = \sigma_R^2 + \sigma^2(I_s). \tag{21}$$

Using equations (20) and (21) we find

$$\bar{I}_s = \sqrt{\bar{I}^2 - \sigma_R^2} = \sqrt{2\bar{I}^2 - \overline{I^2} + \sigma^2(I_s)}. \tag{22}$$

In practice, the values of $\bar{I}^2$ and $\overline{I^2}$ are obtained from the first-order statistics of the intensity. To find the value of $\sigma^2(I_s)$ the power spectrum is partitioned. The Rician variance σ_R^2 is estimated as the area under the Gaussian fit to the minima of the spectrum. Since the total area under the power spectrum is equal to $\sigma^2(I)$, $\sigma^2(I_s)$ can be estimated using equation (21). I_d then follows from $I_d = \bar{I} - \bar{I}_s$.

The following tissue characterizing parameters were used: the average intensity due to structure normalized to the intensity due to diffuse scattering ($\bar{I}_s/I_d$), and the variable component of the intensity due to structure normalized to the intensity due to diffuse scattering ($\sigma(I_s)/I_d$).

Pronounced peaks in the power spectrum, corresponding to the distance d between the regularly spaced scatterers (namely the structured scattering), were located. Only periodicities larger than the resolution of the transducer and smaller than 3 mm were considered. The distances corresponding to the peaks were averaged (Insana *et al* 1986) with weighting factors equal to the difference between the spectral peak value and the value of the Gaussian fit at that frequency.

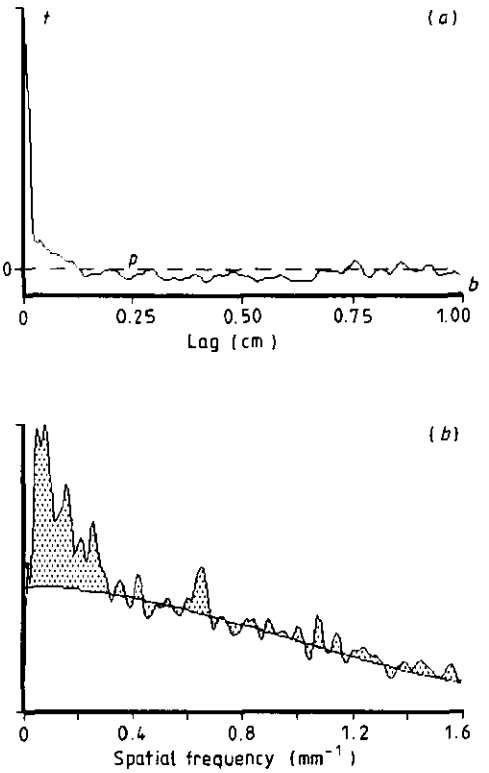

Figure 2. Axial autocorrelation function (*a*) and corresponding noise power spectrum (*b*) of the intensity image of a ROI of a healthy liver. The Gaussian spectrum of the Rician noise is also shown in (*b*). The abscissae are in arbitrary units (*t*, *p* and *b*: see text).

3. Methods

3.1. Data acquisition equipment

To be able to record the RF signals *in-vivo* a conventional echo scanner was interfaced to a transient recorder and a microcomputer. A preliminary version of the equipment used was described in detail before (Kruimer *et al* 1985). The system was controlled by a personal computer (PRO380, Digital Equipment Inc.) which was also used for the storage of the recorded RF signals. As the ultrasonic front-end a mechanical sector scanner (Sonoline 3000, Siemens Inc.) was used, equipped with a transducer with a fixed focal distance ($F = 7.5$ cm, $f_c = 3.0$ MHz, $\Delta f_{1/2} = 0.94$ MHz). On the screen of the scanner a region-of-interest (ROI), with variable position and size, was made visible for the selection of homogeneous portions of the tissue. After the operator pressed a switch, the RF signals corresponding to the selected ROI were recorded during a single scanning motion of the transducer. The recorded RF signals were digitized and intermediately stored by a transient recorder (BE256, Bakker Electronics), which operated at 12 MHz sampling rate and had a resolution of 8 bit. The RF signals were amplified by the TGC (time-dependent gain control) amplifier of the scanner, but were not logarithmically compressed.

During data acquisition the quality of the recorded RF data was assessed on-line by performing an initial analysis using an array processor (VAP64B, DSP Inc.). If

the number of segments where the RF signal caused overflow in the transient recorder was higher than 25%, the operator was automatically alerted to either change the setting of the TGC or to avoid strong reflectors. After each recording session the data were transferred to a PDP 11/34 computer (Digital Equipment Inc.) on which further analysis was performed off-line.

Before any analysis of the data was performed the depth-dependent amplification was removed from the signals. For this purpose the steering voltage of the TGC amplifier, which corresponds to a certain amplification factor, was also digitized and stored in addition to the RF signals. The relationship between the steering voltage and the amplification was measured by recording the RF echo signals of a tissue phantom at a number of steering voltage levels. The spectra of these echoes were calculated and normalized with respect to the spectrum corresponding to one of the steering voltage levels (1 V), thus yielding the relative amplification factor as a function of frequency and of steering voltage. No significant frequency dependence of the amplification was observed. The relationship between steering voltage and amplification, however, appeared to be depth-dependent (i.e. depending on time with respect to the transmission pulse). Therefore, this dynamic relationship was established in 13 successive non-overlapping zones, each 8 mm in depth, thus yielding 13 look-up tables (LUT). Correction was carried out by dividing the sampled amplitudes of the RF lines by the amplification factor corresponding to the steering voltage value recorded for that sample at the same depth.

3.2. Measurement of the diffraction spectrogram

The average transfer function $D^2(f, z)$ due to diffraction and focusing was measured by estimating the spectra of the echo signals from a tissue-mimicking phantom at a range of depths. The phantom consisted of degassed water in which 5% gelatin was dissolved at 60 °C. A powder consisting of fine carbon particles was stirred through the gelatin solution after which it was allowed to congeal during continuous slow rotation for 6 h. The density of scatterers was approximately 10^5 cm^{-3}, and the attenuation coefficient was (0.15 ± 0.02) dB cm^{-1} MHz^{-1}.

The phantom was placed in a tank filled with degassed water at room temperature, and for every depth the transducer was repositioned in such a way that the recorded echo signals came from the same volume in the phantom, just below the top surface (figure 3). To prevent disturbances caused by multiple reflections in the water tank the electronics of the scanner was modified so that only one pulse was transmitted during each sector scanning motion of the transducer. The direction of propagation of the sound pulse was perpendicular to the top surface of the phantom.

For each depth 100 independent RF lines were recorded by moving the transducer in a plane parallel to the top surface of the phantom. This procedure was repeated 38 times each time increasing the distance between the transducer and the sampling volume in the phantom by 4 mm.

From the recorded RF signals a time-gated segment of 128 samples, corresponding to 8 mm of depth, was selected just beyond the surface reflection of the phantom for each of the depth ranges at which measurements were taken. In this way the time-gated segments of consecutive depths overlapped by 50%. The amplitude spectra of the segments were calculated after multiplication with a Hanning window (Oppenheim and Schafer 1975). The 100 spectra corresponding to the 100 transducer positions were then ensemble averaged for each of the 38 depths. This yielded the spectrogram corresponding to equation (8). The spectra were then normalized with respect to

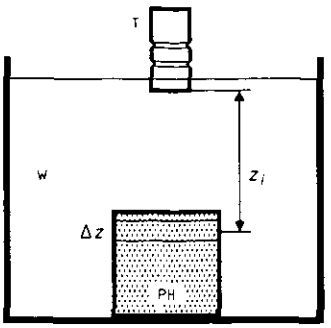

Figure 3. Experimental set up used to measure the depth dependent properties of the sound beam. (t = transducer, ph = phantom, w = water)

the spectrum obtained for the focal zone, resulting in the correction spectrogram of equation (9), the inverse of which is shown in figure 4. Outside the usable bandwidth the filter values were made equal to 1. Correction of a 128-sample depth segment of a RF signal was performed by dividing its spectrum by the normalized spectrum of the filter corresponding to the same depth as explained in section 2.1. The influence on the sound beam caused by the water standoff (cf figure 3) was neglected. The attenuation at the acoustic path length within the phantom, being the same for all distances z_i, was also neglected. In figure 4 the change in spectral shape with depth is clearly visible.

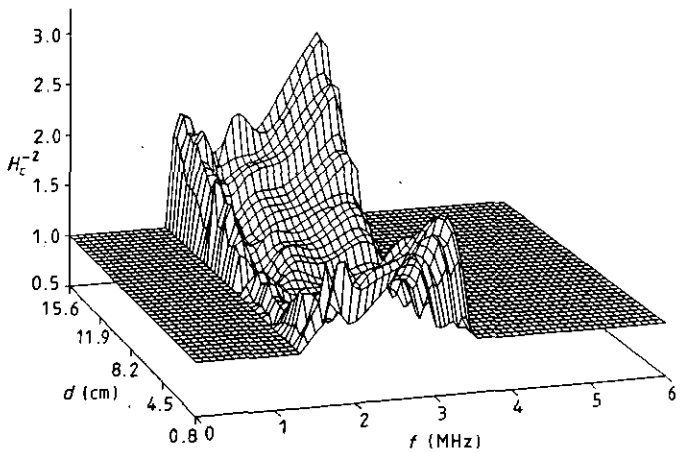

Figure 4. The inverse of the diffraction amplitude spectrogram relative to the spectrum at the focal distance (cf equation (11)), which is used for the correction for the depth-dependent sound beam properties. d = distance to the transducer in cm, f = frequency in MHz.

3.3. Computer simulations

Computer simulated echograms were obtained by using the simulation program described in its preliminary form by Cloostermans (1984) and in its complete form by

Romijn *et al* (1989). In the simulation program a tissue model was employed consisting of randomly positioned point scatterers in a homogeneously attenuating medium. The attenuation was modelled to be linear with frequency ($\alpha(f) = \beta f$) using the causal attenuation transfer function derived by Gurumurthy and Arthur (1982), which was also applied for the correction for attenuation (see section 2.3). For the present application the scattering process was assumed to be frequency independent. The model was one-dimensional and therefore sound beam effects of the transducer were not included. The transmitted pulse was modelled as having a Gaussian envelope. The centre frequency of the pulse was 3 MHz and the standard deviation of the (also) Gaussian amplitude spectrum corresponding to this pulse was 0.4 MHz. The simulated echograms each consisted of 50 completely independent RF lines, corresponding to a depth of 4 cm at a sound velocity of 1550 m s^{-1}. Simulations were performed with ten values of the attenuation coefficient inserted, ranging from 0.1 to 1.0 dB cm^{-1} MHz^{-1}. For each value of the attenuation coefficient six simulated echograms were obtained, which sums up to a total of 60 simulated scans consisting of 50 independent RF lines each.

3.4. Phantom measurements

Using our data acquisition equipment, RF scans were recorded of a tissue-mimicking phantom (Nuclear Associates†). Several scans were taken at a number of depths of the region of interest and at a number of adjustments of the TGC. The manufacturer specified the attenuation coefficient of the phantom as 0.5 dB cm^{-1} MHz^{-1}. The phantom contained wires and holes, but these were carefully avoided, so that only RF data corresponding to homogeneous parts of the phantom were acquired.

3.5. Clinical study

In this study we have examined patients as well as volunteers. The volunteers (group I, $N = 74$, age: 30 ± 8 y), who were partly recruited from the personnel of our departments, were examined to obtain normal values of the parameters. Because the majority of these volunteers was between 17 and 33 y of age we additionally scanned a group of patients (group II, $N = 48$, age: 46 ± 16 y), most of which were older than 33 y. The patients in this group were in general referred to the Radiology Department for an echographic examination of their kidneys, on suspicion of kidney stones or dilatation of the pelvic system. Both the volunteers and the patients in these groups did not have a history of liver disease, had only minimal intake of alcohol and there were no clinical signs of liver disease. All these volunteers and patients had an echographic liver examination following standard procedures, during which no liver pathology was assessed.

A third group consisted of patients having a diffuse liver pathology (group III, $N = 39$, age: 50 ± 14 y). In particular, we considered cirrhosis, a disease which causes the replacement of parenchymal tissue by collageneous tissue. Several kinds of cirrhosis proved by biopsy were included in this group such as cirrhosis caused by alcoholic abuse, cirrhosis on basis of chronic hepatitis and primary biliary cirrhosis. Also patients suffering from storage diseases, (i.e. Wilson's disease and haemochromatosis), were included. These patients did not have a fatty liver.

With our measurement equipment at least eight independent ROIs from each patient, or volunteer, were selected and recorded. The scanning was usually done subcostally and the ROIs were chosen in the right lobe of the liver. During the selection

† Address: PO Box 1000, 55 North Street, Freeport, NY 11520, USA.

of the ROIs care was taken to choose only homogeneous parts of the liver and to avoid strong reflections, caused by for example large blood vessels, as well as possible. The size of the ROI could be changed if neccessary, but in general the largest scans possible were taken. After positive visual assessment of the frozen image and when no substantial overflow was detected, the RF signals were stored in the computer.

3.6. Processing of the RF signals

Since the analysis methods are based on a homogeneous tissue model, all local structures, which correspond to deviations from the model (e.g. blood vessels, diaphragm) were detected so that they could be omitted during the analysis. The analysis of every recorded RF scan was started with the detection of segments where the signals caused overflow of the transient recorder, and segments where the signals were to weak to be properly analysed. This detection was performed in 128-sample depth segments that overlapped by 50%. The remaining relatively strong reflections and relatively low echo areas were detected by comparing the signal power in every depth segment of each RF line with the power in that depth segment ensemble averaged over all the RF lines in the ROI. During the calculation of the ensemble averaged power, the segments containing overflow and the segments with a signal that was too weak were omitted. Segments with a signal power larger than 1.75 times and lower than 0.25 times the average power at the same depth were detected. These factors were experimentally established by visually comparing the marked regions with the reconstructed B-mode image for 200 scans of the liver. All the segments that were marked were left out of the analysis. If more than 20% of the segments was marked the ROI was not further analysed. If more than 20% of an A line was marked the line was not used for second-order texture analysis. If the line was used for this purpose, the marked segments were filled with the average amplitude.

After the RF signals were corrected for the TGC the estimates of the attenuation coefficient were obtained using the methods described in section 2.2. Then the envelope was calculated after the depth dependencies caused by attenuation and the properties of the sound beam were corrected for. The value of the attenuation coefficient estimated with the log-power decay method was used for the correction. The attenuation coefficient of the intervening liver tissue was assumed to be the same as that of the interrogated tissue. Correction for the attenuation in the intervening liver tissue was only performed for the distance beyond 5 cm from the transducer (z_0 in equations (18) and (19)). The intervening skin, subcutaneous fat and muscle tissues were assumed to fill a fixed range of 5 cm just beyond the transducer in all patients. It was assumed that the influences of these tissues on the echo signals were the same in all patients (i.e. slope of the attenuation coefficient 0.5 dB cm^{-1} MHz^{-1} (NCRP 1983)). Therefore, they were not corrected for.

To prevent amplification of noise by the attenuation correction procedure prior to the envelope detection, we additionally applied a band limiting spectral window function which caused the corrected spectra to approach zero smoothly at 0.4 and at 3.8 MHz (i.e. the boundaries of the unattenuated pulse spectrum). Finally, any remaining long-range trends in the echo envelope signal due to inhomogeneity of the tissue were removed by correcting the envelope detected scan lines with a smoothed version (i.e. the trend) of the ensemble averaged envelope. The size of the smoothing window was chosen to be large enough to prevent local amplitude variations to be included in this trend. We used a triangular-shaped window the size of which was approximately 20 times the transmitted pulse length. The detrending did not change

the (global) average amplitude of the ROI and it did not influence the local amplitude differences.

4. Results

4.1. Simulations: comparison of attenuation estimation methods

The five methods used to estimate the frequency-dependent attenuation coefficient that were described in section 2.2 were tested and compared using the simulated RF data described in section 3.3. Because beam properties were not included in the simulated model, the diffraction correction was omitted in this case. For each simulated RF scan consisting of 50 independent lines the attenuation coefficient was estimated. The results are shown in figure 5 in which the average value of the estimated attenuation coefficient minus the value inserted in the simulations is displayed as a function of the inserted value. The error bars represent one standard deviation calculated from six simulated echograms. These figures show that the accuracy with which the attenuation coefficient was estimated does not depend on its absolute value. This result is in accordance with equation (14).

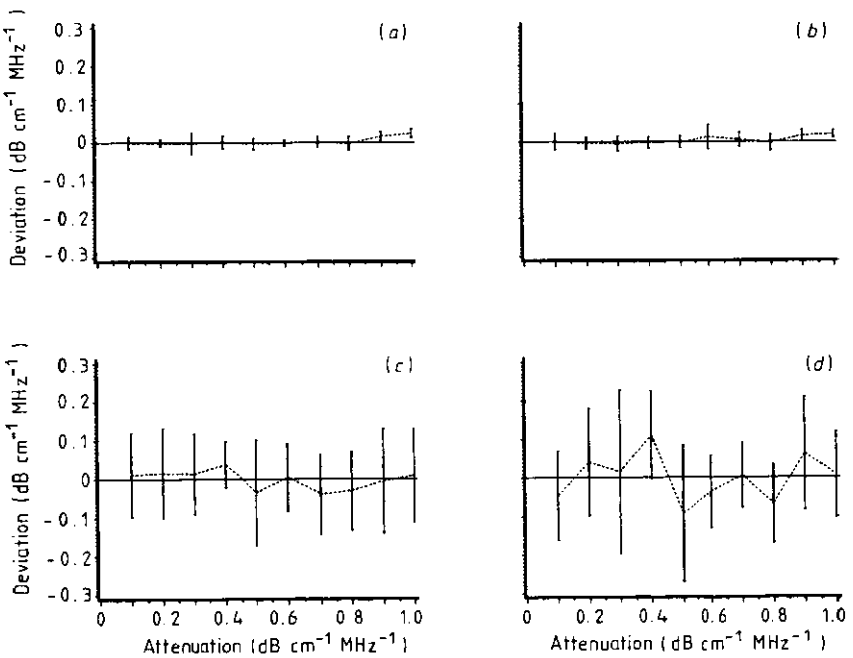

Figure 5. The difference between estimated and true (i.e. simulated) attenuation coefficient for estimation methods: (*a*) LPD, (*b*) MNB$_0$, (*c*) CFS and (*d*) MNB-α_1 (section 2.2). Bars indicate ± one standard deviation.

In table 1 the properties of the estimation methods are summarized. It shows the average values of the differences between the estimated and the true value of the attenuation coefficient ($\alpha_{est} - \alpha_{true}$) and the standard deviation of this difference. Also

Table 1. The average difference between the estimated and true attenuation parameters, the standard deviation of this difference (s), and average standard deviation ($\bar{s}$) of the estimate obtained from the fitting procedure using one scan (precision). Averaging was performed over 60 simulated scans. In the last column the theoretical value of the precision is given. (β and α_1 in dB cm−1 MHz−1; α_0 in dB cm−1; α in dB cm−1 MHz^{-n}).

Method	Parameter	Est−true	s	$\bar{s}$	$\bar{s}_t$
LPD	β	0.003	0.017	0.036	0.011
CFS	β	−0.002	0.104	0.23	0.07
MNB_0	β	0.004	0.020	0.009	0.015
MNB	α_0	0.03	0.41	0.21	0.17
	α_1	−0.01	0.15	0.08	0.07
	$\alpha(\bar{f})/\bar{f}$	0.004	0.023		
MNB_p	α	0.09	0.27	0.08	0.06
	n	−0.11	0.53		$0.166/\alpha(\bar{f})$
	$\alpha(\bar{f})/\bar{f}$	0.01	0.02		

shown is the standard deviation obtained per scan from the fitting procedure, using the 50 RF lines each scan consists of, averaged over all 60 simulations ($\bar{s}$).

The log-power decay (LPD) method as well as the multi-narrowband method using a frequency fit with zero intercept (MNB_0) yielded accurate estimates of the true value of the attenuation coefficient. The bias, estimated by the average deviation from the true value, was small 0.003 ± 0.020 dB cm^{-1} MHz^{-1} for both methods. The standard deviation per scan (using the 50 independent RF lines per scan) was also small, 0.036 and 0.009 dB cm^{-1} MHz^{-1} respectively.

The centroid frequency shift (CFS) method yielded a smaller overall bias but the accuracy and precision of a single estimation were bad. A larger number of scans is needed to obtain a reliable average value of the attenuation coefficient. The standard deviation of the difference between the estimated and true value was a factor five larger than with the MNB_0 and LPD methods.

The remaining two MNB methods, the first using the frequency fit without the intercept forced to zero (MNB) and the second using the exponential fit (MNB_p), are less accurate methods because two parameters have to be found from the fitting procedures. For the MNB method the average deviation of the intercept α_0 from zero, which was inserted in the simulation, was 0.03 ± 0.41 dB cm^{-1}. The average difference between the estimated and the true value of the slope of the attenuation coefficient was equal to -0.01 ± 0.15. The precision per scan was not high: $\bar{s}_{\alpha_0} = 0.21$ and $\bar{s}_{\alpha_1} = 0.08$. For the MNB_p method the coefficient α was estimated with a bias of 0.09 ± 0.27 dB cm^{-1} MHz^{-1} and the exponent was on average underestimated $n = 0.90 \pm 0.53$. The precision using only one scan was low: $\bar{s}_\alpha = 0.08$ and $\bar{s}_n$ was dependent on the attenuation at the central frequency and ranged from 0.78 (theory: 0.66) at 0.1 dB cm^{-1} MHz^{-1} true attenuation to 0.08 (theory: 0.07) at 1.0 dB cm^{-1} MHz^{-1} true attenuation. When the inserted value of the attenuation coefficient was below 0.3 dB cm^{-1} MHz^{-1} the errors in α and n became very large. Although both methods allow more general information about the tissue to be obtained, more data are needed to reduce the variability of the results.

The latter two MNB methods both allow the estimation of a summary parameter. For the MNB method this summary parameter is $\alpha_{f_c} = (\alpha_0 + \alpha_1 f_c)/f_c$ and for the MNB_p method it is $\alpha_{f_c} = (\alpha f_c^n)/f_c$. This latter parameter was also employed by Parker

et al (1986). These parameters which are also included in table 1 yielded accuracies and precisions which are comparable with the MNB_0 and LPD methods.

To find out whether the methods yielded independent estimates of the attenuation coefficient the correlation coefficients between the estimates of the methods was evaluated (table 2). For this purpose we again first subtracted the true attenuation coefficient from the estimated value.

Table 2. Correlations of the attenuation coefficients estimated using five different methods ($p < 0.05$) on simulated data (cf table 1). An asterisk indicates that the correlation was not significant.

Method		CFS	MNB_0	MNB			MNB_p		
		β	β	α_0	α_1	$\alpha(\bar{f})/\bar{f}$	α	n	$\alpha(\bar{f})/\bar{f}$
LPD	β	*	0.74	−0.36	0.46	0.44	−0.25	0.29	0.40
CFS	β		−0.35	*	*	−0.37	*	*	−0.32
MNB_0	β			*	*	0.86	*	*	0.81
MNB	α_0				−0.99	0.61	0.79	−0.73	0.91
	α_1					−0.51	−0.78	0.72	−0.51
	$\alpha(\bar{f})/\bar{f}$						0.51	−0.43	0.95
MNB_p	α							−0.91	0.55
	n								−0.48

The most striking result is that the estimates of the CFS method, which is exclusively based on frequency information, were not highly correlated with those estimated with the other methods. The estimates of the LPD method, which only uses amplitude information, also only showed a low correlation with the other methods except for the MNB_0 method (0.74). The coupled parameters α_0 and α_1 of the MNB method and α and n of the MNB_p method showed high mutual correlations (−0.99 and −0.91, respectively). However, these parameters did not show high correlation with the estimates of the LPD, CFS and MNB_0 methods. The summary parameters of the MNB and MNB_p methods introduced previously and the estimate of the MNB_0 method also showed a high correlation. Since the averages and standard deviations (table 1) were also the same these parameters are equivalent. All three MNB methods utilize both amplitude and frequency information.

4.2. Performance of the correction procedures

To test the methods used to correct for diffraction effects, attenuation and TGC, the RF data obtained from a tissue-mimicking phantom (section 3.4) were used. The attenuation coefficient was estimated using all the methods described in section 2.2. Only the results for the MNB_0 method are shown, but similar results were obtained using any of the other methods. Figure 6 shows the estimated attenuation coefficient as a function of the distance of the ROI to the transducer. An inadequate correction for the TGC or for the diffraction and focusing would have caused a depth dependence of the estimated attenuation coefficient. Since the estimated value showed no such trend, and assuming that the tissue-mimicking phantom was homogeneous, we may conclude from these measurements that the correction procedures yield satisfying results. The overall average of the estimated attenation coefficient is 0.63 dB cm^{-1} MHz^{-1}, which

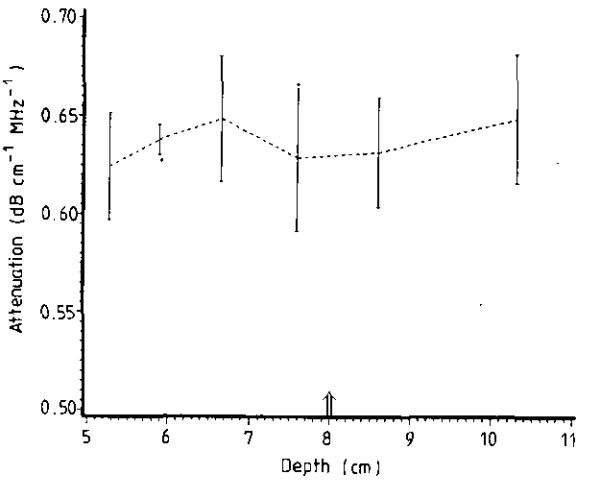

Figure 6. The attenuation coefficient (MNB$_0$ method) as a function of the depth of the ROI in the phantom. ROI size was 40 RF lines of length 4 cm. Bars indicate ± one standard error of the mean. The arrow indicates the focus.

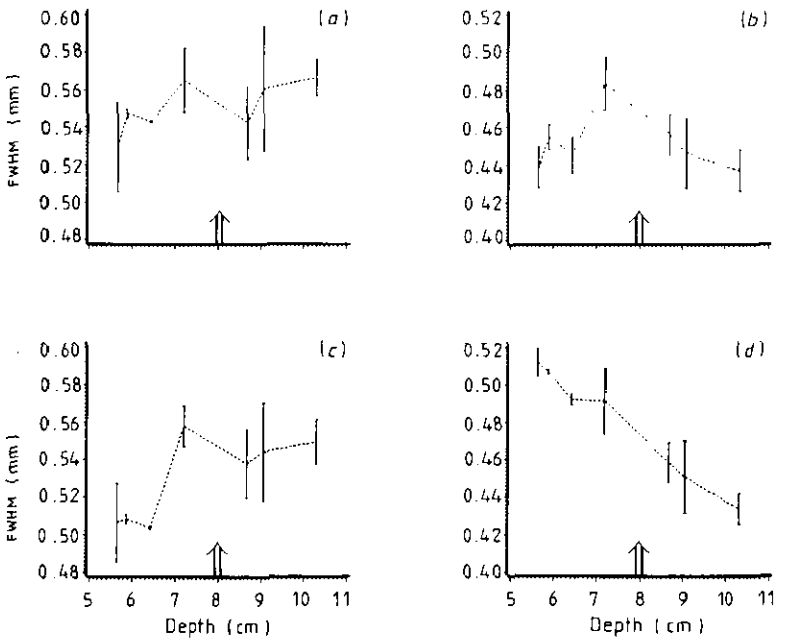

Figure 7. The FWHM of the axial autocovariance function estimated from the envelope of the RF signals obtained from a tissue-mimicking phantom: (*a*) corrections for attenuation and diffraction effects; (*b*) no corrections; (*c*) correction for attenuation only; and (*d*) correction for diffraction only. Bars indicate ± one standard error of the mean. The arrows indicate the focus.

is higher than the value of 0.5 dB cm^{-1} MHz^{-1} specified by the manufacturer. This difference may be the consequence of aging caused by the phantom drying out.

Figure 7 shows the full width at half maximum (FWHM) of the autocovariance

function (section 2.4) in the axial direction for four situations: no corrections applied (figure 7(*b*)), correction for diffraction and attenuation (figure 7(*a*)) correction for diffraction only (figure 7(*d*)) and correction for attenuation only (figure 7(*c*)). When no corrections were performed the FWHM increased until the focal zone and decreased beyond. When only the diffraction correction was employed the FWHM in front of the focal zone was increased to the level at the focal distance, but beyond this distance a decrease was still present. When the diffraction correction was omitted and only the frequency-dependent correction for the attenuation was applied the reverse was true. If both diffraction effects and the attenuation were corrected for, an almost depth independent estimation of the FWHM was achieved. The unexpected decrease beyond the focus in figures 7(*b*) and 7(*d*) is caused by the asymmetrical non-Gaussian spectrum of the pulse of the transducer under influence of the attenuation. The unattenuated pulse spectrum is biased towards the higher frequencies. The attenuation, being stronger at higher frequencies, changes the spectrum in such a way that it becomes more symmetrical with an *increased* −6 dB bandwidth, and therefore, a *smaller* FWHM. Since the deviations from the average value were smaller than the standard deviation of the estimate at each depth we may conclude that the corrections adequately remove the depth dependencies.

4.3. Average results of clinical measurements

4.3.1. Attenuation estimates. The results of the attenuation analysis obtained from these three groups of human subjects are presented in table 3. This table includes the number of subjects and the average age of the subjects within the groups. For all the parameters and estimates the population average and standard deviation are presented. In addition, the results of a *t*-test for comparison between the groups are given. The average attenuation coefficient value found for the volunteers with a normal liver is in agreement with values reported in the literature (Taylor *et al* 1986, Garra *et al* 1987a, b). The LPD, MNB_0 and the MNB (α_1) methods yielded approximately the same values. For the normal volunteers (first group) the averages were 0.49 ± 0.07, 0.50 ± 0.05 and 0.51 ± 0.11 dB cm^{-1} MHz^{-1} respectively. The differences between these methods were very small, although the MNB (α_1) parameter showed a spread which was twice that of the MNB_0 estimate. When the centroid frequency shift (CFS) method was used we obtained a value which was larger: 0.53 ± 0.08 dB cm^{-1} MHz^{-1}. The second group of subjects with a normal liver (patients) showed attenuation estimates which were on average higher than in the first group: 0.53 ± 0.07 dB cm^{-1} MHz^{-1}. However, the value obtained with the CFS method was lower: 0.50 ± 0.11 dB cm^{-1} MHz^{-1}. The results of the various estimation methods obtained for the group of patients with a diffuse liver disease were very consistent: 0.55 dB cm^{-1} MHz^{-1}. The spread in this group was, however, a factor two to three higher than in the normal liver groups. This caused a considerable overlap of the three groups.

In all three groups the zero intercept (α_0) of the MNB method was approximately zero, although a large spread was found. Large population standard deviations were also found for the two parameters obtained with the MNB_p method using the power law fit. The power was approximately the same for the three groups, and equalled 1.0. The parameter α was the same for the second normal liver group and the liver pathology group, but was lower in the first normal liver group. To reduce the large spread of the estimates of α and n, which was also found for the simulations, averaging the results of more independent scans would be needed for every patient. The cause

Table 3. Averages of the attenuation parameters in each of the clinical groups. The standard deviation of the parameter within the group is also given. The furthest right columns show the results of a t-test for comparison between the groups. Only values of p less then 0.10 have been reproduced. (β and α_1 in dB cm^{-1} MHz^{-1}; α_0 in dB cm^{-1}; α in dB cm^{-1} MHz^{-1}.)

Method		Volunteers Normals (I)	Patients (II)	Liverpathology group (III)	t-test $p > \|t\|$ I–II	I–III	II–III
N		74	48	39			
Age		30 ± 8	46 ± 16	50 ± 14			
LPD	β	0.49 ± 0.07	0.53 ± 0.08	0.55 ± 0.19	0.001	0.06	
CFS	β	0.53 ± 0.08	0.50 ± 0.11	0.55 ± 0.13			
MNB_0	β	0.50 ± 0.05	0.53 ± 0.07	0.55 ± 0.17	0.010	0.06	
MNB	α_0	-0.03 ± 0.29	0.04 ± 0.32	-0.01 ± 0.39			
	α_1	0.51 ± 0.11	0.52 ± 0.14	0.55 ± 0.15			
MNB_p	α	0.52 ± 0.15	0.59 ± 0.14	0.59 ± 0.29	0.009		
	n	1.03 ± 0.22	0.96 ± 0.25	1.03 ± 0.26			

of this large spread must be found in the attenuation model, with which more detailed information can be obtained at the cost of less precision, and in the relatively small bandwidth available.

The attenuation coefficient only showed a limited capability to discriminate between the different clinical groups (table 3: t-test results). Using the LPD and MNB_0 estimates it was possible to significantly differentiate ($p < 0.06$) group I from group III. Using the same estimation methods a significant difference ($p < 0.01$) was also found between the two normal groups (I and II). It was, however, not possible to differentiate significantly between groups II and III.

When comparing the estimation methods the correlation coefficients should also be considered. These were calculated for the pooled data, that is for all three groups treated as a single group, and are presented in table 4. The results presented here confirm to a large extent the results of the simulations. Unlike the result found for the simulations a high correlation was found between the LPD estimate and the MNB_p-α parameter. Here the CFS estimate also correlated with the MNB-α_1 parameter.

Table 4. Correlations of the attenuation parameters obtained using five different estimation methods ($p < 0.025$) on all clinical scans. An asterisk indicates that the correlation was not significant.

Method		CFS	MNB_0	MNB		MNB_p	
		β	β	α_0	α_1	α	n
LPD	β	0.44	0.98	0.39	0.36	0.82	−0.32
CFS	β		0.61	−0.39	0.78	*	0.43
MNB_0	β			0.23	0.53	0.71	*
MNB	α_0				−0.71	0.82	−0.96
	α_1					−0.20	0.72
MNB_p	α						−0.76

It should be noted that the correlation coefficients found for the simulations display the mutual dependence of the estimation methods more accurately, because the true attenuation coefficient was subtracted. In the *in-vivo* situation this was not possible since the true attenuation coefficient was not known. In this situation the

correlation coefficients yielded higher values, although the estimation methods still may be independent to some extent.

4.3.2. Texture parameters. In table 5 the population averages and standard deviations of the parameters calculated from the corrected envelope signals (A-mode lines) are summarized. The *t*-test results for comparison between the groups are also presented. All four parameters from the first-order statistics appear to supply information about the condition of the interrogated tissues. The mean amplitude found in the group of liver patients was on average a factor of two higher (*t*-test: $p < 0.02$) than in the normal groups. The large spread, however, indicates the heterogeneity of this group, probably caused by including several kinds of pathology. The SNR values also show considerable overlap, which resulted in less significant differences between the groups.

Table 5. Averages of the texture parameters in each of the clinical groups. The standard deviation of the parameter within the group is also given. The columns furthest right show the results of a *t*-test for comparison between the groups. Only values of p less then 0.10 have been reproduced. (μ in arbitrary units; FWHM and $\bar{d}$ in mm.)

Method	Volunteers Normals (I)	Volunteers Patients (II)	Liver pathology group (III)	$p > \|t\|$ I–II	$p > \|t\|$ I–III	$p > \|t\|$ II–III
μ	25 ± 5	30 ± 9	55 ± 62	0.006	0.006	0.015
SNR	2.00 ± 0.05	2.02 ± 0.06	2.04 ± 0.06	0.002	0.03	
$\bar{I}_s/I_d$	0.37 ± 0.14	0.47 ± 0.16	0.55 ± 0.21	0.0001	0.0002	0.08
$\sigma(I_s)/I_d$	0.45 ± 0.06	0.50 ± 0.05	0.51 ± 0.06	0.0001	0.0001	
FWHM	0.45 ± 0.01	0.44 ± 0.02	0.44 ± 0.02			
$\bar{d}$	1.46 ± 0.36	1.45 ± 0.38	1.52 ± 0.38			

The parameters $\bar{I}_s/I_d$ and $\sigma(I_s)/I_d$, which characterize the properties of the structural and diffuse components of the scattered intensity showed on average significant differences (*t*-test: $p < 0.0002$) between groups I and II and between groups I and III. A wide overlap existed, however, between the liver pathology group (III) and the second normal liver group and to a lesser extent the first normal liver group.

The second-order texture parameters do not appear to represent information that can be useful for the discrimination between the groups. The axial speckle size, characterized by the FWHM of the axial autocovariance function yielded, on average, the same value in all three groups and showed only a small spread. The spread in the parameter $\bar{d}$, which characterized the distance between structured scatterers, was so large that the differences between the averages in the normal group and the liver pathology group appeared to be insignificant (*t*-test).

In table 6 the mutual correlations between the texture parameters are presented. The parameter $\bar{I}_s/I_d$ showed a high positive correlation with the SNR (0.83), which confirms the observations of Tuthill *et al* (1988) based on a simulation study. Mutually the two parameters representing structure, $\bar{I}_s/I_d$ and $\sigma(I_s)/I_d$, were also highly correlated (0.84). The other correlation coefficients were very small, indicating that the parameters are mutually independent.

To obtain the parameters $\bar{I}_s/I_d$ and $\sigma(I_s)/I_d$ the square root in equation (22) (section 2.4) had to be evaluated. The estimate of the argument of the square root was, however, sometimes negative, in which case no real solution exists. The number of recorded RF scans for which the square root could be evaluated expressed as a

Table 6. Correlations of the texture parameters ($p < 0.025$) obtained from the clinical data. An asterisk indicates that the correlation was not significant.

	SNR	$\overline{I}_s/I_d$	$\sigma(I_s)/I_d$	FWHM
μ	*	*	*	*
SNR		0.83	0.53	−0.27
$\overline{I}_s/I_d$			0.84	*
$\sigma(I_s)/I_d$				0.21

percentage of the total number of scans recorded for a patient is denoted by p_I. p_I was on average only 55% in the first normal liver group which means that for 45% of the scans the parameters $\overline{I}_s/I_d$ and $\sigma(I_s)/I_d$ could not be evaluated. In the other two groups p_I was larger: 72% in the second normal liver group and 79% in the liver patient group.

The number p_I correlated with the SNR (0.85) and with $\overline{I}_s/I_d$ (0.64), which means that, keeping in mind the results of Tuthill *et al* (1988), the chance of obtaining an estimation of the parameters $\overline{I}_s/I_d$ and $\sigma(I_s)/I_d$ increases if the strength of the structural component increases.

In only approximately 70% of the power spectra of the intensity obtained per patient could significant peaks, which are supposed to indicate the distance between regularly spaced scatterers, be detected. This might be caused by the poor resolution of the echographic transmission pulse (0.75 mm). Another plausible explanation is that the structure was too irregular to be detected as such. Furthermore, the hexagonal cylindrical liver lobules are mostly not irradiated perpendicularly to the cylinder axes, which causes a large spread in distances between the structural scatterers as they are observed in the scan plane. The contribution of the structure is then distributed over more spatial frequencies and the peaks in the spectrum become too small to be detected.

4.3.3. Correlation between texture and attenuation parameters. Interaction processes between the ultrasound and the tissue exist, which influence both attenuation and texture properties. If the strength of the scattering, which is the most important process, increases, the mean amplitude and the attenuation coefficient are increased as well. This was observed, for example by Garra *et al* (1987a), in livers with steatosis (bright liver). Therefore, the attenuation coefficient and the mean amplitude correlate although the envelope signals were corrected for the (frequency-dependent) attenuation. Table 7 shows the correlation coefficients (> 0.15) between the attenuation estimates and the first- and second-order texture parameters. Indeed the mean amplitude showed positive correlation to the estimates of the attenuation coefficient based on amplitude information (LPD) and to a lesser extent to the estimates based on mixed frequency-amplitude information, obtained with the MNB methods. The estimates obtained from the CFS method showed only a low correlation with the mean amplitude.

The second-order texture parameter FWHM showed a small negative correlation with the attenuation estimates, which must be attributed to insufficiencies in the correction methods.

All correlation coefficients not shown in table 7 were smaller than 0.15.

Table 7. Mutual correlations (> 0.15) between texture and attenuation parameters ($p < 0.025$) obtained from the clinical data.

Method	LPD	CFS	MNB_0	MNB		MNB_p
	β	β	β	α_0	α_1	α
μ	0.68	0.36	0.66	0.25	0.25	0.57
FWHM	−0.40	−0.33	−0.44	−0.16	−0.18	0.33

5. Discussion

It has been well established that, in order to obtain a depth independent estimate of the attenuation and scattering parameters, corrections have to be carried out for the ultrasonic beam properties. It was investigated to which extent these beam properties influenced the texture of the B-mode images (Oosterveld *et al* 1985). In an attempt to correct the images by a deconvolution with the two-dimensional RF point spread function it was found to be only feasible if certain system requirements are fulfilled (Jeurens *et al* 1987). In practice these requirements are usually not met and, therefore, several other methods have been tried which are less complicated. For example, Morris (1988), carried out corrections on the estimated parameters using a look-up table for each parameter which was established using the parameters of the whole population averaged at each depth. Zuna *et al* (1987) corrected the images themselves, but when using their method only the mean amplitude becomes depth independent, provided the appropriate TGC correction was applied. The problem with these methods is that in order to obtain a depth independent texture the influence of the attenuation also has to be taken into account. Although the TGC of the ultrasound scanner was used to correct the amplitude decay, the influences on the second-order statistical properties of the texture were not corrected for in the latter two papers.

Using the method presented in section 2.3 we were able to correct to a great extent the depth dependencies of the A-mode texture, with respect to the first-order and axial second-order statistical properties. The obtained estimates of the texture parameters are, however, not device independent because the transmission pulse properties were not removed by deconvolution and a correction was only applied relative to the focal zone to yield depth independence. The method can be further refined if the distance z_0 (cf equations (16) and (17)) is specified for each separate scan and a correction is carried out for the attenuation in the intervening muscle and skin tissues. Corrections for the influence of the sound beam and the attenuation on the lateral texture properties are still subject to further investigations (Thijssen *et al* 1989).

We have tested several attenuation estimation methods and several models for the frequency dependence of the attenuation coefficient. Non-linearity of this dependence has been shown before to play a role only at higher ultrasound frequencies and when using a broadband transmission pulse (Lin *et al* 1987). We found that, using our equipment with its low central frequency transmission pulse and its relatively small bandwidth, it was practically impossible to significantly distinguish the frequency dependence of the attenuation coefficient from the linear $\alpha(f) = \beta f$ model. Three estimation methods (LPD, MNB_0 and CFS) were used which are based on the linear model. The estimates obtained with the CFS method, which is exclusively based on frequency information, were found to be not significantly dependent of the estimates obtained using methods based on amplitude information (LPD and MNB_0). This result

was also found by Tsao *et al* (1987) and by Romijn (1990). All the methods are unbiased although averaging over independent scans is needed to obtain sufficient precision. In the simulation study the CFS method yielded a population standard deviation which was five times larger than for the LPD and MNB_0 methods. This difference was not found in the clinical study.

Although the methods were designed to estimate the attenuation coefficient, the estimation results may be influenced by other properties of the interrogated tissue than the attenuation. The extent to which this happens, however, is dependent on the estimation method, i.e. the employed tissue model may not be adequate. The CFS method, for example, is influenced by the frequency dependence of scattering (Romijn *et al* 1989). The allowance of a non-zero intercept for the frequency dependence of the attenuation coefficient (MNB method) has been indicated to take the presence of specular scatterers and reflectors into account (Laugier *et al* 1985). It should therefore be remarked that the testing of the methods using simulated RF data with a linear frequency dependence of the attenuation coefficient does not exclude any method from being useful for the *in-vivo* situation.

The attenuation coefficient showed a limited capability to discriminate between the different clinical groups. Only by using the LPD and MNB_0 estimates was it possible to significantly differentiate between the normal livers of a relatively young group of healthy volunteers (group I) and pathologic livers (group III). Using the same estimation methods a significant difference was also found between group I and an older group of patients who were assumed to have a healthy liver (group II). However, in a more recent study we have addressed the dependence of the attenuation, and also the texture parameters, on the age of the subjects. Significant correlations have been found (Hartman *et al* 1991a) and after correction of the parameters of groups I and II for these age dependencies a homogeneous population of normal subjects resulted (Hartman *et al* 1991b). It was not possible to significantly differentiate between groups II and III using the attenuation coefficient. The estimates of both methods show a high mutual correlation, so that it is not advisable to use more than one of these methods in a discriminant analysis. The CFS method did not yield estimates of the attenuation which could significantly differentiate the clinical groups previously mentioned. The large standard deviations obtained for the liver pathology group (III) may be attributed to the inclusion of several kinds of pathology The discriminating power might be improved by a subclassification of this group, which will be possible when we have collected more patients in each subgroup.

In this study we have limited ourselves to only a few statistical texture parameters that can be related to physical properties of the examined tissues, such as the scattering strength (μ), the density of scatterers (μ, SNR, FWHM) (Oosterveld *et al* 1985) and the relative strength of the structural and random scattering ($\overline{I}_s/I_d$, $\sigma(I_s)/I_d$, SNR) (Wagner *et al* 1986, Wagner *et al* 1988, Tuthill *et al* 1988) and the average distance between structured scatterers (Insana *et al* 1986). Other (*ad hoc*) statistical measures which may also yield discriminating power (Raeth *et al* 1985, Nicholas *et al* 1986, Morris 1988) can be estimated from the texture, but were not used in this study. We have only found significant discriminating power ($p < 0.05$) for the first-order statistical texture parameters (μ, SNR, $\overline{I}_s/I_d$, $\sigma(I_s)/I_d$). The mean amplitude (μ) was approximately a factor of two higher in pathologic livers compared with healthy livers. The spread in values found in group III was, again, very large due to the heterogeneity of this group. When using the SNR, $\overline{I}_s/I_d$, and $\sigma(I_s)/I_d$ significant differences were found between groups I and II and between groups I and III. These parameters, however,

showed a relatively high mutual correlation. All three parameters were increased in the case of liver pathology, which would mean that an increase in structural scattering is present. The dependence of the SNR on structural scattering was investigated by Tuthill *et al* (1988). These authors found a large increase in the SNR if the echoes from the structured scatterers positively interfered ($\bar{d} = n\lambda$, with $n = 1, 2, \ldots$, and λ the wavelength).

The estimated average scatterer spacing ($\bar{d}$) is, on average, larger in the case of liver pathology, but the spread in the values found in the three groups is so large that this parameter does not contribute any significant discriminating power. The only second-order statistical parameter included in this study, was the axial speckle size characterized by the FWHM of the axial autocovariance function. This parameter was shown to be sensitive to changes in the density of scatterers (Oosterveld *et al* 1985) as long as the density remained below the Rayleigh limit set by the ultrasonic equipment. Since this parameter yielded approximately the same value in all three groups, the conclusion may be drawn that the density of scatterers was in general above the Rayleigh limit. So the changes observed in the SNR have to be completely attributed to changes in structural scattering.

Elsewhere the authors showed that the spread in the estimated values was, next to the expected interindividual variability, caused by intraindividual variability (Oosterveld 1990, Hartman *et al* 1991a). The estimates changed during the day due to the circadian rhythm. The estimates obtained on separate days but at the same time of the day also showed a variability. Nevertheless, the results presented in tables 3 and 5 indicate that a discrimination between normal livers and pathologic livers may well be possible. In addition, the results of the t-test are probably too pessimistic and may improve if the heterogeneous liver pathology group can be subclassified based on biopsy results and other clinical findings. A paper on the subject of retrospective discriminant analysis based on the parameters obtained using the discussed methods is in preparation (Hartman *et al* 1991b).

Acknowledgments

This work has been supported by a grant of the Technical Science Branch of the Netherlands' Organization for Scientific Research and was performed within the framework of the Concerted Action Programme on Ultrasonic Tissue Characterization and Echographic Imaging of the European Communities (COMAC BME, DG XII).

References

Berger G, Laugier P, Fink M and Perrin J 1987 Optimal precision in ultrasound attenuation estimation and application to the detection of Duchenne muscular dystrophy carriers *Ultrason. Imag.* 9 1–17

Cloostermans M J T M 1984 A-scan simulation program *Ultrasonic Tissue Characterization and Echographic Imaging* 3 ed J M Thijssen and K Irion (Nijmegen: Faculty of Medicine Printing Office)

Cloostermans M J T M, Mol H, Verhoef W A and Thijssen J M 1986 *In vitro* estimation of acoustic parameters of the liver and correlations with histology *Ultrasound Med. Biol.* **12** 39–51

Cloostermans M J T M and Thijssen J M 1983 A beam corrected estimation of the frequency dependent attenuation of biological tissues from backscattered ultrasound *Ultrason. Imag.* **5** 136–47

Ferrari L and Jones J P 1985 The propagation of Gaussian modulated pulses in dissipative and/or dispersive media such as tissue *Ultrasound Med. Biol.* **11** 299–305

Fink M A and Cardoso J F 1984 Diffraction effects in pulse-echo measurement *IEEE Trans. Sonics Ultrason.* **SU-31** 313–29

Fink M, Hottier F and Cardoso J F 1983 Ultrasonic signal processing for *in vitro* attenuation measurement: short time Fourier analysis *Ultrason. Imag.* **5** 117–35

Garra B S, Insana M F, Shawker T H and Russell M A 1987a Quantitative estimation of liver attenuation and echogenicity: normal state *versus* diffuse liver disease *Radiology* **162** 61–7

Garra B S, Shawker T S, Insana M F and Wagner R F 1987b *In vivo* attenuation measurement methods and clinical relevance *Ultrasonic Tissue Characterization and Echographic Imaging* **6** ed J M Thijssen and G Berger (Luxembourg: Commission of the EC)

Gurumurthy K V and Martin Arthur R 1982 A dispersive model for the propagation of ultrasound in soft tissue *Ultrason. Imag.* **4** 355–77

Hartman P C, Oosterveld B J, Thijssen J M and Rosenbusch G J E 1991a Variability of quantitative echographic parameters of the liver: intra- and inter-individual spread, circadian rhythms and age related effects *Ultrasound Med. Biol.* submitted

—— 1991b Retrospective classification of diffuse liver disease by quantitative echography (in preparation)

Insana M F 1983 Improvements in the spectral difference method for measuring ultrasonic attenuation *Ultrason. Imag.* **5** 331–45

Insana M F, Wagner R F, Garra B S, Brown D G and Shawker T H 1986 Analysis of ultrasound image texture via generalized Rician statistics *Opt. Eng.* **25** 743–8

Jeurens T J M, Somer J C, Smeets F A and Hoeks A P G 1987 The practical significance of two-dimensional deconvolution in echography *Ultrason. Imag.* **9** 106–16

Kak A and Dines K A 1978 Signal processing of broad band pulsed ultrasound: measurement of attenuation in soft biological tissues *IEEE Trans Biomed. Eng.* **BE-25** 321–44

Kruimer W H, Lammers J H E and Thijssen J M 1985 Ultrasonic Biopsy Apparatus *Acoustical Imaging* **14** ed A J Berkhout, J Ridder and L F van der Wal (New York: Plenum)

Kuc R 1985 Bounds on estimating the acoustic attenuation of small tissue regions from reflected ultrasound *Proc. IEEE* **73** 1159–68

Kuc R and Schwartz M 1979 Estimating the acoustic attenuation coefficient slope for liver from reflected ultrasound signals *IEEE Trans. Sonics Ultrason.* **SU-26** 353–62

Kuc R, Schwartz M and Von Micsky L 1976 Parametric estimation of the acoustic attenuation coefficient slope for soft tissue *IEEE Ultrasonics Symposium Proceedings* (IEEE Cat No 76 CH11200-SSU) 44–7

Laugier P, Berger G, Fink M and Perrin J 1985 Specular reflector noise: effect and correction for *in-vivo* attenuation estimation *Ultrason. Imag.* **7** 277–95

Lin T, Ophir J and Potter G 1987 Frequency dependent ultrasonic differentiation of normal and diffusely diseased liver *J. Acoust. Soc. Am.* **82** 1131–8

Morris D T 1988 An evaluation of the use of texture measurements for the tissue characterization of ultrasonic images of *in vivo* human placentae *Ultrasound Med. Biol.* **14** 387–95

NCRP 1983 *Biological Effects of Ultrasound: Mechanisms and Clinical Applications* NCRP Report 74

Nicholas D, Nassiri D K, Garbutt P and Hill C R 1986 Tissue characterization from ultrasound B-scan data *Ultrasound Med. Biol.* **12** 135–43

Oosterveld B J 1990 On the quantitative analysis of ultrasound signals with applications to diffuse liver disease *PhD Thesis* University of Nijmegen

Oosterveld B J, Thijssen J M and Verhoef W A 1985 Texture of B-mode echograms: 3-D simulations and experiments of the effects of diffraction and scatterer density *Ultrason. Imag.* **7** 142–60

Oppenheim A V and Schafer R W 1975 *Digital Signal Processing* (Englewood Cliffs, NJ: Prentice-Hall)

Parker K J 1986 Attenuation measurement uncertainties caused by speckle statistics *J. Acoust. Soc. Am.* **80** 727–34

Parker K J, Asztely M S, Lerner R M, Schenk E A and Waag R C 1988 *In-vivo* measurements of ultrasound attenuation in normal or diseased liver *Ultrasound Med. Biol.* **14** 127–36

Raeth U, Schlaps D, Limberg B, Zuna I, Lorenz A, Van Kaick G, Lorenz W J and Kommerell B K 1985 Diagnostic accuracy of computerized B-scan texture analysis and conventional ultrasonography in diffuse parenchymal and malignant liver disease *J. Clinical Ultrasound* **13** 87–9

Romijn R L 1990 On the quantitative analysis of ultrasound signals and applications to intraocular melanomas *PhD Thesis* University of Nijmegen

Romijn R L, Thijssen J M and Van Beuningen G W J 1989 Estimation of scatterer size from backscattered ultrasound: a simulation study *IEEE Trans. Ultrason. Ferroel. Freq. Contr.* **UFFC-36** 593–606

Shaffer S, Pettibone D W, Havlice J F and Nassi M 1984 Estimation of the slope of the acoustic attenuation coefficient *Ultrason. Imag.* **6** 126–38

Taylor K J, Riely C A, Hammers L, Flax S, Weltin G, Garcia-Tsao G, Conn H O, Kuc R and Barwick K W 1986 Quantitative US attenuation in normal liver and in patients with diffuse liver disease: importance of fat *Radiology* **160** 65–71

Thijssen J M, Oosterveld B J and Fabel R 1989 Diffraction correction: the lateral point of view *Ultrason. Imag.* **11** 129–30

Tsao J W, Morimura S, Itoh H, Itoh I and Konishi T 1987 Comparisons of images derived from amplitude, mean frequency and attenuation coefficient of pulse echo signals *Japan. J. Med. Ultrasonics* **14** 393–406

Tuthill T A, Sperry R H and Parker K J 1988 Deviations from Rayleigh statistics in ultrasonic speckle *Ultrason. Imag.* **10** 81–9

Verhoef W A, Cloostermans M J T M and Thijssen J M 1985 Diffraction and dispersion effects on the estimation of ultrasound attenuation and velocity in biological tissues *IEEE Trans. Biomed. Eng.* **BE-32** 521–9

Wagner R F, Insana M F and Brown D G 1986 Unified approach to the detection and classification of speckle texture in diagnostic ultrasound *Opt. Engng.* **25** 738–42

Wagner R F, Insana M F and Smith S W 1988 Fundamental correlation lengths of coherent speckle in medical ultrasonic images *IEEE Trans. Ultrason. Ferroel. Freq. Contr.* **UFFC-35** 34–44

Whalen A D 1971 *Detection of Signals in Noise* (New York: Academic)

Zuna I, Volk J, Raeth U, Schlaps D, Naves W, Lorenz A, Lorenz D, Van Kaick G and Lorenz W J 1987 TC-System influence on the B-mode image features *Ultrasonic Tissue Characterization and Echographic Imaging* vol 6 ed J M Thijssen and G Berger (Luxembourg: Commission of the EC)